Partial Respiratory Motion Compensation for Abdominal Extracorporeal Boiling Histotripsy Treatments With a Robotic Arm

Gilles P. L. Thomas, Tatiana D. Khokhlova, and Vera A. Khokhlova

***Abstract*— Extracorporeal boiling histotripsy (BH), a noninvasive method for mechanical tissue disintegration, is getting closer to clinical applications. However, the motion of the targeted organs, mostly resulting from the respiratory motion, reduces the efficiency of the treatment. Here, a practical and affordable unidirectional respiratory motion compensation method for BH is proposed and evaluated in *ex vivo* tissues. The BH transducer is fixed on a robotic arm following the motion of the skin, which is tracked using an inline ultrasound imaging probe. In order to compensate for system lags and obtain a more accurate compensation, an autoregressive motion prediction model is implemented. BH pulse gating is also implemented to ensure targeting accuracy. The system is then evaluated with *ex vivo* BH treatments of tissue samples undergoing motion simulating breathing with the movement of amplitudes between 5 and 10 mm, the frequency between 16 and 18 breaths/min, and a maximum speed of 14.2 mm/s. Results show a reduction of at least 89% of the value of the targeting error during treatment while only increasing the treatment time by no more than 1%. The lesions obtained by treating with the motion compensation were close in size and affected area to the no-motion case, whereas lesions obtained without the compensation were often incomplete and had larger affected areas. This approach to motion compensation could benefit extracorporeal BH and other histotripsy methods in clinical translation.**

***Index Terms*— Histotripsy, motion compensation.**

I. Introduction

EXTRACORPOREAL high-intensity focused ultrasound (HIFU) treatments have been shown to be a promising noninvasive alternative for tumor ablation in the liver [1], [2], breast [3], [4], pancreas [5], [6], and kidney [2], [7]. Targeting of the extracorporeal HIFU treatment is usually performed with ultrasound imaging or magnetic resonance imaging (MRI) [8]. In ultrasound imaging guidance, the diagnostic probe is usually located at the center of the transducer and is axially aligned with its focus, referred to as an inline imaging probe.

Using HIFU, different methods of tissue ablation are possible, such as thermal ablation, where long—in the range of hundreds of milliseconds to seconds—ultrasound pulses delivered at high duty cycle elevate the temperature through absorption at the focus up to 70 °C [9]. Recently, several methods of mechanical tissue ablation were developed, where short (microseconds to milliseconds) high-amplitude ultrasound pulses delivered at low duty cycle generate intense bubble activity at the focus resulting in tissue fractionation [10], [11]. In particular, boiling histotripsy (BH) uses millisecond-long pulses of highly nonlinear HIFU waves to heat the focus up to boiling temperature, forming an mm-sized vapor bubble that interacts with the remaining pulse resulting in tissue liquefaction [12], [13].

However, the physiological motion of the organs, mainly resulting from respiration, can cause a time-varying offset between the targeted tissue and the transducer focus and, thus, have a negative impact on the precision and safety of HIFU treatment. For thermal ablation, this means a reduction in the treatment efficiency [14], and in both mechanical modalities of ablation, this motion has been shown *in vivo* to cause larger, irregularly shaped lesions [15]–[18]. The possibility of damage to adjacent healthy tissues is a safety concern with all treatment modalities.

Multiple ways of mitigating the physiological motion during HIFU treatment have been proposed over the years. The simplest method was to maintain breath hold during treatment, either self-induced [19] or under general anesthesia and mechanical ventilation [20]; however, as a consequence, the treatment time was substantially increased [21]. Treatments can be also performed during continuous breathing but require motion tracking of the targeted tissue. This tracking can either be implemented using visual tracking of the skin surface [22], [23], MRI [24], [25], maintaining isoforce contact with the skin [26], or ultrasound imaging [27]–[29]. Once the motion is properly estimated, it can be accounted for passively by

Manuscript received March 4, 2021; accepted April 23, 2021. Date of publication April 27, 2021; date of current version August 27, 2021. This work was supported by NIH under Grant R01EB007643, Grant R01GM122859, Grant RO1EB025187, Grant P01DK043881, and Grant RSF 20-12-00145. *(Corresponding author: Gilles P. L. Thomas.)*

Gilles P. L. Thomas is with the Applied Physics Laboratory, Center for Industrial and Medical Ultrasound, University of Washington, Seattle, WA 98105 USA (e-mail: gillespierre.thomas@gmail.com).

Tatiana D. Khokhlova is with the Division of Gastroenterology, School of Medicine, University of Washington, Seattle, WA 98195 USA.

Vera A. Khokhlova is with the Applied Physics Laboratory, Center for Industrial and Medical Ultrasound, University of Washington, Seattle, WA 98105 USA, and also with the Physics Faculty, Moscow State University, 119991 Moscow, Russia.

This article has supplementary downloadable material available at https://doi.org/10.1109/TUFFC.2021.3075938, provided by the authors.

Digital Object Identifier 10.1109/TUFFC.2021.3075938

respiratory gating [23], i.e., the HIFU is only turned on when the focus is aligned within a certain margin to the targeted tissue. However, this method increases the treatment time and reduces its efficiency. Another method is to implement active motion compensation using robots that follow the tracked target, effectively canceling most of the motion [22], [26], [28], [29]. Alternatively, active compensation using a multielement HIFU transducer in the pulse–echo mode for the motion tracking and correcting for it by steering the focus electronically was also proposed [30]. However, this method requires a transducer with a large number of elements for proper tracking and steering.

All the methods of motion compensation described above were originally designed for thermal HIFU treatments, in which long HIFU pulses interfere with ultrasound imaging, such that interleaved ultrasound imaging and HIFU sonication sequences had to be developed [28], [29]. Unlike thermal HIFU, histotripsy uses infrequent short pulses; therefore, the problem of synchronizing HIFU bursts and imaging is not as critical.

Some of the prior studies on using ultrasound imaging for motion estimation employed real-time speckle-tracking algorithms in the region of HIFU focus for precise displacement estimation [28], [29]. Implementation of these algorithms for extracorporeal histotripsy *in vivo* is complicated by several factors that are challenging to overcome. First, due to the large water-filled standoff typical for extracorporeal HIFU setups, the distance from the imaging probe to the HIFU focus is usually quite large (120 mm in the present case). This large distance combined with a relatively small imaging array aperture often restricted by the size of the central opening (40 mm in our setup) usually results in a low signal-to-noise ratio (SNR), thus complicating real-time speckle tracking algorithms. Furthermore, out-of-plane motion results in decorrelation of speckles [31], which makes them more prone to generating false motion estimates. These issues were overcome by Seo *et al.* [32], [33] by implementing motion tracking in 3-D but required the addition of a second imaging system and probe to the setup and a sophisticated algorithm. Another successful method to enhance speckle tracking capability during thermal HIFU treatments was based on tracking the hyperechoic region that gradually appears at the HIFU focus with tissue coagulation [33]. However, this approach is unlikely to be effective in histotripsy because changes in tissue echogenicity at the focus are rapid (on the order of milliseconds) and transient due to the high speed and vorticity of residual bubble motion through liquefied tissue [18].

Other previous works on active motion compensation are tracked and compensated for the movement of skin closest to the organ of interest [22], [26]. In the case of extracorporeal HIFU setups, the interface between coupling water (completely anechoic) and skin represents a steep contrast change on the B-mode imaging, making it an easy and reliable reference to track. However, the motion of the liver due to respiration in the porcine model and humans is complex and dependent on the part of the organ targeted [34], [35], and as such, tracking the skin would only allow for partial, unidirectional compensation of its motion. In both humans and pigs, generally, the dominant liver motion components are cranio–caudal and anterior–posterior. Both motion components are dependent on the specific lobe and the subject's position, and the exact reported displacement values vary widely, within 10–25 mm (humans) and 2–5 mm (pigs) for the cranio–caudal direction and 2.5–12 mm (humans) and 1–10 mm (pigs) for anterior–posterior direction [34], [35]. The former cannot be compensated with the unidirectional method proposed here, only the latter.

In this article, we present an active unidirectional respiratory motion compensation method using a robotic arm that is adapted to histotripsy, specifically BH. The objective was to develop a method that would be affordable and relatively generic in its implementation for use in ongoing *in vivo* BH treatments of the liver in porcine models and humans in the future. The capabilities of the method were evaluated by performing BH ablations of *ex vivo* tissue undergoing quasi-periodic motion replicating pig respiration: the amplitude of the motion ranged between 5 and 10 mm, the frequency of around 17 breaths/min, and speeds within 5–14 mm/s.

II. Materials and Methods

A. HIFU Transducer, Imaging Probe, and Robotic Arm

A 1.5-MHz, 256-element array designed to deliver abdominal BH treatments [36]–[38] made of piezoelectric composite material (Imasonic, Voray sur l'Ognon, France) was used in this study and is shown in Fig. 1. The element's diameter was 7 mm; and the transducer had a nominal focal distance of 120 mm, an outer diameter of 144 mm, and a central opening of 40-mm diameter, where a coaxial ultrasound imaging probe (ATL P6-3) was set. The transducer was designed for extracorporeal BH treatments and, as such, could generate the required high-amplitude shock fronts (up to 100 MPa) at the focus at the peak acoustic power of 275 W in water. The transducer was driven by a four-board V1 Verasonics research system (V-1 Ultrasound Acquisition platform, Verasonics Inc, Kirkland, WA, USA) with an HIFU option.

The 128-element phased array imaging probe was connected to a separate two-board V1 Verasonics system. The B-mode ultrasound imaging acquisition was made using a transmit at 4.5 MHz and a sampling frequency $F_s = 18$ MHz, and the reconstruction was made using 36 scan lines focused at the same depth as the transducer, 120 mm, and distributed in a rectangular area directly in front of the imaging probe array of 34 mm-width and 135-mm depth, with a frame rate of 27.5 Hz.

The HIFU array with the inline imaging probe was then attached to a robotic arm (UR3e, Universal Robots, Odense, Denmark) using a custom 3-D-printed holder, as shown in Fig. 1. The robotic arm was a six-degree-of-freedom cobot, i.e., specifically designed for human interaction, and had a 500-mm reach, a maximum payload weight of 3 kg, repeatability of movement of ± 0.03 mm, and a maximum speed of 1 m/s. The arm was mounted on tripod support with retractable wheels.

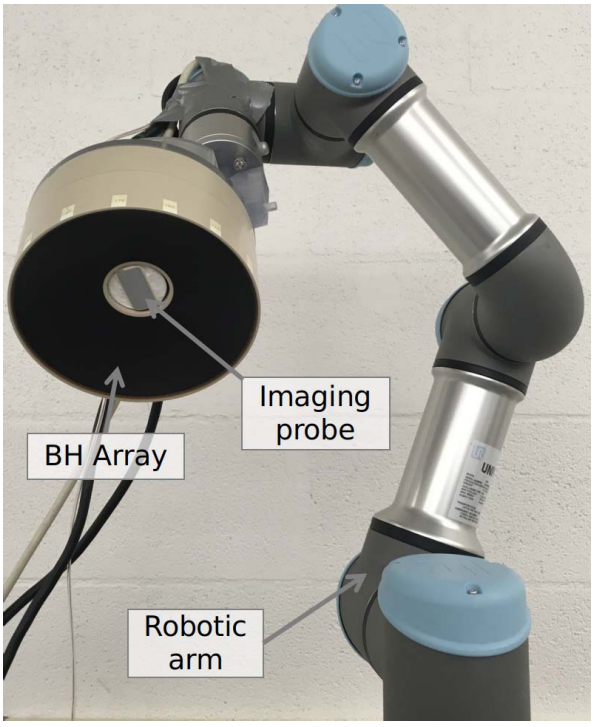

Fig. 1. Photograph of the BH transducer array with inline imaging probe mounted on the robotic arm.

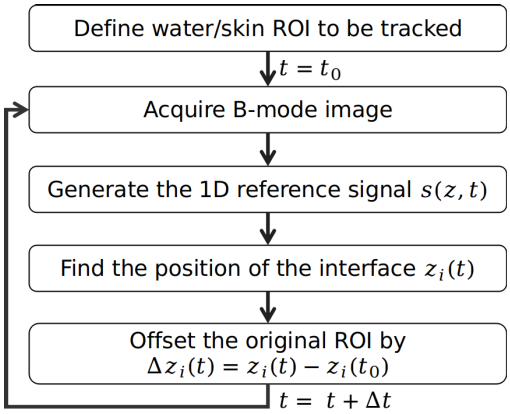

Fig. 2. Flow diagram of the water/skin interface tracking algorithm.

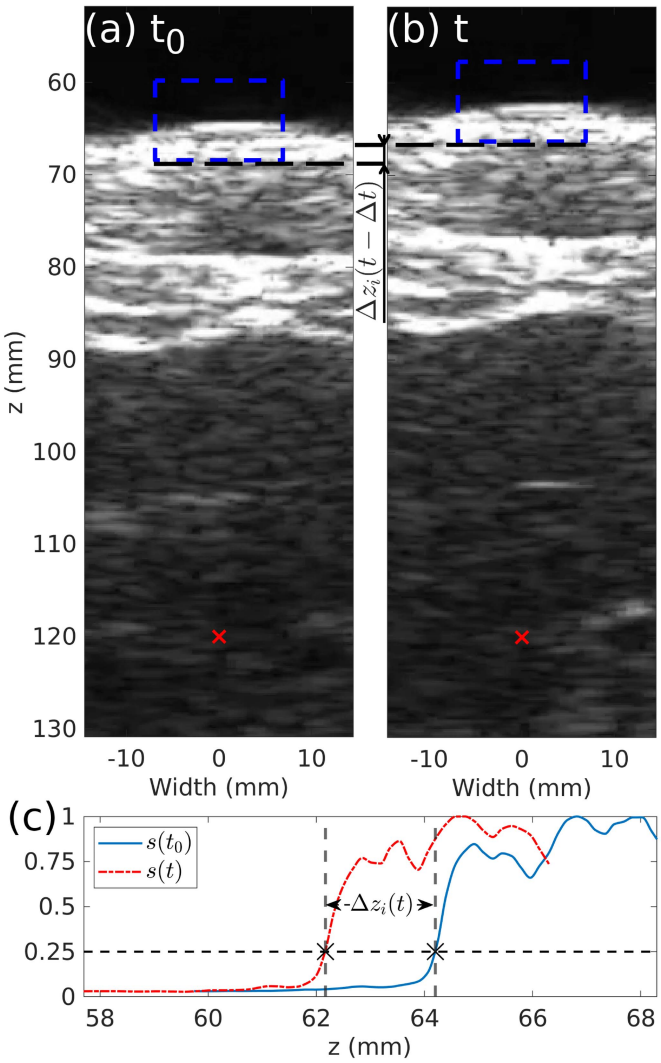

Fig. 3. (a) and (b) B-mode images taken with the inline imaging probe during an *in vivo* BH treatment of the liver of a pig in free-breathing condition, where the boxes in ▬ represent the ROI to be tracked and the red cross is the focus of the transducer. Here, $t - t_0 = 1$ s. (c) Normalized 1-D signals from the ROI in (a) ▬ and (b) ▬ used in the tracking algorithm. The threshold value T is represented by ▬.

B. Motion Tracking

The approach to track the motion of the water/skin interface along the axis of propagation of the HIFU transducer and imaging probe, referenced as z, is described in this section. The ultrasound imaging-derived signal used in the tracking algorithm was similar to that presented by Chanel *et al.* [28] and is illustrated with a diagram in Fig. 2. An example of the implementation of the tracking algorithm on a free-breathing pig during an independent prior *in vivo* BH liver treatment is shown in Fig. 3. A region of interest (ROI), including the water–skin interface, was selected on the B-mode image (illustrated as dashed blue boxes in Fig. 3(a) and (b)). The brightness values of the pixels along the transverse dimension were then summed and normalized to generate a 1-D signal, as shown in Fig. 3(c), which was used for the tracking. Here, the ROI enclosed the interface between the water and the skin, with its width and height chosen such that the interface contrast change on the 1-D signal could be easily tracked with a certain threshold value over the entire respiratory cycle. In some cases where the contrast change was not steep enough, the 1-D signal was also squared to improve the signal contrast. This 1-D signal was then interpolated by a factor of 16 with a piecewise cubic Hermite interpolation to increase its sampling rate to 288 MHz in order to improve the resolution of the tracking. This resulting signal will be referred to as $s(z,t)$, where z is the imaging depth relative to the imaging probe and t is the time.

Once a suitable signal $s(z,t)$ had been generated from the B-mode image, tracking of the interface position was performed by choosing an adequate threshold T that allows to track the surface smoothly and using a zero-crossing detection on the signal $s(z,t)-T$ to find the position $z_i(t)$ corresponding to distance of the water/skin interface relative to the imaging probe, as shown in Fig. 3(c). The value of T was chosen as slightly above the maximum amplitude of the noise in

front of the water/skin interface. The displacement $\Delta z_i(t) = z_i(t) - z_i(t_0)$ of the interface relative to its initial value, where t_0 is the time that the tracking algorithm was initialized, was defined. Finally, in order to ensure that the same interface was tracked continuously over a long time, the ROI of the tracking algorithm was translated by $\Delta z_i(t)$, therefore making the ROI follow the interface, as illustrated in Fig. 3(a) and (b).

C. Motion Prediction

The output of the displacement estimation described above could theoretically serve as direct input to the robotic arm for motion compensation. However, the lags stemming from the limited B-mode imaging frame rate (27.5 Hz in the present case), the execution time of motion tracking algorithm, the communication between the different modules (ultrasound imaging, computers, and the robot), and limited acceleration of the robotic arm (the safest, and therefore, most restrictive setting for acceleration was used here) would accumulate (over 100 ms in the present case) and could lead to less accurate and, thus, less efficient motion compensation, even with an appropriately tuned controller, as demonstrated by another group [39]. One solution to this problem is the use of motion prediction algorithms in tandem with motion estimation. Motion prediction methods rely on *a priori* knowledge of some of the motion characteristics. For example, the free-breathing motion in both anesthetized pigs and humans is known to be almost periodic, with only small variations of the motion period and amplitude between each breath [40], [41]. In this study, a time-varying seasonal autoregressive (TVSAR) prediction model, originally developed for the motion prediction of lung tumors during radiotherapy [42], was used.

The TVSAR model is based on the seasonal autoregressive (SAR) model used to model time series with periodical variations. The SAR model is given as follows:

$$\Delta z_i(t) = \epsilon(t) + \sum_{\delta=1}^{n} \Phi_\delta \cdot \Delta z_i(t - \delta p) \tag{1}$$

where Φ_δ, $\delta = 1, 2, \ldots, n$ are the SAR coefficients, n is the order of the SAR model, $\epsilon(t)$ is a Gaussian white noise with zero mean and variance σ^2, and p is the period. To obtain future prediction for a h-time ahead, the prediction model becomes

$$\Delta \hat{z}_i(t + h \mid t) = \sum_{\delta=1}^{n} \hat{\Phi}_\delta \cdot \Delta z_i(t + h - \delta p) \tag{2}$$

where $\Delta \hat{z}_i(t+h \mid t)$ is the predicted value of $\Delta z_i(t+h)$ at the instant t, and $\hat{\Phi}_\delta$ is the estimated value of Φ_δ. Equation (2) allows for predicting future values of Δz_i as a weighted sum of its previous values for n periods back.

The TVSAR model allows for small variations in period by replacing the term δp in (1) and (2) by the reference intervals $r_\delta(t)$, and thus, the prediction model becomes

$$\Delta \hat{z}_i(t + h \mid t) = \sum_{\delta=1}^{n} \hat{\Phi}_\delta \cdot \Delta z_i(t + h - r_\delta(t)). \tag{3}$$

The values of the reference intervals $r_\delta(t)$ represent the local period of the δth breath. At the initialization of the algorithm, a recording of length T_i of the respiration motion containing a known number of $N \geq n$ breath periods is obtained, resulting in an estimated period of $p = T_i N^{-1}$. The following correlation function CF is then defined as:

$$\mathrm{CF}(t, k) = \int_0^p (\Delta z_i(t-\tau) - \mu) \cdot (\Delta z_i(t-k-\tau) - \mu)\, d\tau \tag{4}$$

where k is a lag value and μ is the mean of $\Delta z_i(t)$ over the interval $[t - T_i, t]$. The values of the reference interval were then determined by looking at the peak of CF

$$r_\delta(t) = \arg\max_{k \in K_\delta}(\mathrm{CF}(t, k)) \tag{5}$$

where K_δ is the search range for the δth interval, which is set as

$$K_\delta = \left\{ k \mid \delta p - \frac{p}{2} \leq k \leq \delta p + \frac{p}{2} \right\}. \tag{6}$$

Following each time, the values of $r_\delta(t)$ were calculated, and the value of p was replaced such that its value for the next update of the values of $r_\delta(t)$ was the mean of their preceding values:

$$p = \frac{1}{n} \sum_{\delta=1}^{n} r_\delta. \tag{7}$$

Finally, the coefficient Φ_δ of the TVSAR model in 3 was estimated with a recursive least-squares (RLS) filter with forgetting factor [43]. The input and coefficient vectors, $\mathbf{x}(t)$ and $\hat{\mathbf{w}}(t)$, respectively, were set as

$$\mathbf{x}(t) = [\Delta z_i(t - r_1(t)), \ldots, \Delta z_i(t - r_n(t))] \tag{8}$$

$$\hat{\mathbf{w}}(t) = [\hat{\Phi}_1, \ldots, \hat{\Phi}_n] \tag{9}$$

where the initial values of the coefficient vector were set as null

$$\hat{\mathbf{w}}(0) = 0. \tag{10}$$

The update of the values of $\hat{\mathbf{w}}(t)$ was introduced as follows:

$$\hat{\mathbf{w}}(t) = \hat{\mathbf{w}}(t - \Delta t) + \mathbf{R}(t - \Delta t)\mathbf{x}(t - \Delta t)e(t - \Delta t) \tag{11}$$

where $e(t)$ is the error between the filter output and the desired values $z_i(t)$, and $\mathbf{R}(t)$ is the inverse of the autocorrelation matrix, which are calculated as follows:

$$e(t) = z_i(t) - \mathbf{x}(t)\hat{\mathbf{w}}(t - \Delta t)^T \tag{12}$$

$$\mathbf{R}(t) = \frac{1}{\lambda}\left(\mathbf{R}(t-\Delta t) - \frac{\mathbf{R}(t-\Delta t)\mathbf{x}(t)\mathbf{x}(t)^T\mathbf{R}(t-\Delta t)}{\lambda + \mathbf{x}(t)^T\mathbf{R}(t-\Delta t)\mathbf{x}(t)}\right) \tag{13}$$

where λ is the forgetting factor that should be in range from 0 to 1, and with $\mathbf{R}(0) = \gamma \mathbf{I}$, where $\mathbf{I}$ is the identity matrix and γ is a large value (e.g., $\gamma = 10^4$ [43]).

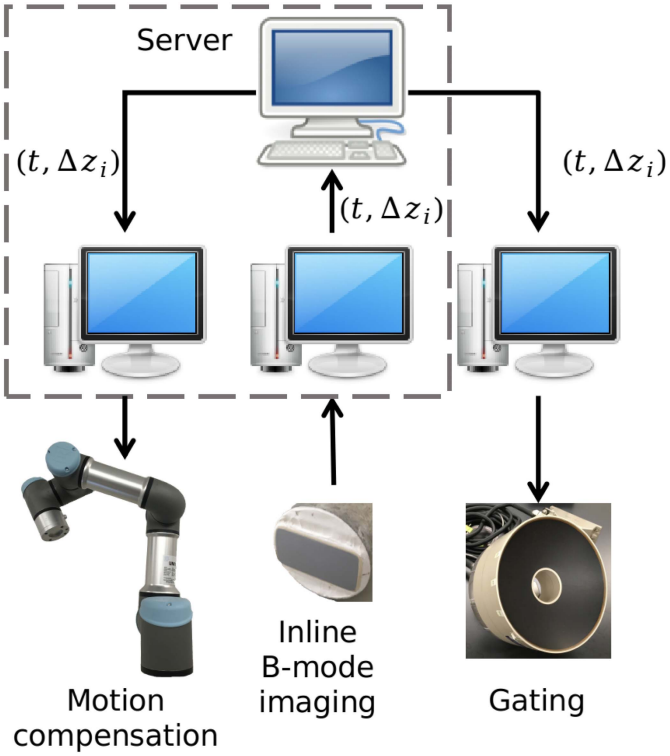

Fig. 4. Diagram of the communications between parts of the respiratory motion compensation and gating system. The - - - frame represents a local host communication.

D. Implementation

The purpose of the setup was to deliver extracorporeal BH treatment while compensating for the respiratory motion and treatment gating in case the compensation was not sufficient. The diagram in Fig. 4 illustrates the communication between the three modules involved in the system: B-mode imaging, the robot controller, and the HIFU transducer array driving module. The data communicated between the modules were: 1) the displacement of water/skin interface, $\Delta z_i(t)$, calculated by the B-mode imaging system as described above and used in the feedback control loop of the robotic arm and, if needed, gating of the HIFU transducer and 2) the time t of the B-mode image acquisition. The data $(t, \Delta z_i)$ from the imaging system were sent by TCP/IP to a server hosted locally on the same computer. This data could be then queried by both the robot controller, also hosted on the same computer, and the HIFU transducer control system hosted on a separate computer.

The displacement estimation was built into the MATLAB Verasonics imaging script as an external process event immediately following the reconstruction event and before the image display event as the display event generated a nonnegligible lag of around 5–10 ms. As soon as the value of Δz_i was obtained, it was sent to the server along with its acquisition time t. Note that, in the current implementation of the system, the 10-ms-long BH pulse emissions were not synchronized with B-mode imaging and could interfere with image acquisition during a pulse. However, given the low pulse repetition frequency (PRF) of 1 Hz, only one B-mode frame per second would potentially be affected. To avoid an arbitrary displacement value resulting from the obstruction of the B-mode by the BH pulse, a check was implemented whether the B-mode image was blocked by the HIFU interference by detecting large sudden changes of the value of z_i, i.e., $|z_i(t) - z_i(t - \Delta t)| \geq \xi$. Here, ξ was set to 1 mm. The value of $z_i(t)$ was then ignored, and instead, its previous value $\Delta z_i(t - \Delta t)$ was sent to the server. The refresh rate of the imaging (27.5 Hz) was fast enough compared to the respiratory motion (<0.4 Hz) that this did not impact the motion compensation.

The gating was also implemented in the MATLAB HIFU Verasonics script as an external process event located just before the BH pulse emission event. The process would query the server and check if the value of $|\Delta z_i|$ was lower than an arbitrarily chosen maximum allowed displacement value ε. If $|\Delta z_i| \geq \varepsilon$, the process would freeze the BH treatment script and query the value of Δz_i with a refresh rate of 100 Hz until it became lower than ε or reached a timeout, which was set here as 10 s. Reaching the timeout would close the treatment program as a protection measure for both the HIFU transducer and the patient.

The server was programed in Python and received the value of $(t, \Delta z_i)$ as a character string that it would then be able to broadcast to other programs when queried with a specific command. The robot controller and the motion prediction algorithm were also programed in Python and communicated to the robotic arm via its proprietary script language (URScript). A control loop, with a refresh rate of 110 Hz, was implemented and was controlling the speed of the robot along the axis of the BH array and inline imaging probe for the motion compensation. Because the B-mode imaging rate of 27.5 Hz, and therefore, the sampling rate of $\Delta z_i(t)$ was significantly lower, they were first resampled using cubic interpolation at 60 Hz and then filtered with a low-pass filter with a cutoff frequency of 5 Hz. The values of $\Delta \hat{z}_i(t + h \,|\, t)$ outside the sampling rate were obtained by cubic interpolation between the two closest samples available.

The values of the coefficient $\hat{\Phi}_\delta$ of the TVSAR model in 3 were calculated using the implementation of the RLS filter available in the Python Adaptive Signal Processing library [44], and the value of the forgetting factor was set as $\lambda = 0.1$. The speed command v_r of the robot was calculated using a discrete proportional derivative controller such that its value was

$$v_r = K_P \Delta \hat{z}_i(t + h|t) + K_D \frac{d \Delta \hat{z}_i}{dt}(t + h|t) \tag{14}$$

where K_P and K_D are the proportional and derivative gain of the discrete controller, respectively. Once the motion prediction program was initialized and the robotic arm was using its output to compensate for the respiratory motion, the value of the displacement fed to the motion prediction algorithm was changed from $\Delta z_i(t)$ to $\Delta \tilde{z}_i(t) = \Delta z_i(t) + \Delta z_r(t)$, where $\Delta z_r(t)$ was the displacement of the robotic arm relative to its initial position.

Finally, software safety was introduced to avoid potential harm to the equipment and personnel. As such, the transducer displacement was limited to a spherical space of radius R_s, and if the robot left this space, it would stop and await a new order. This safety measure was redundant with the hardware

safety settings that were already set at the most restrictive level.

The optimal parameters used for the motion compensation controller were found experimentally as $K_P = 10$ and $K_D = 0.1$. The motion prediction parameter n, corresponding to the number of previous movement periods to be considered for the prediction, should be chosen between 2 and 5 to avoid long calculation of the AR coefficients by the RLS filter. Here, this parameter was set as $n = 3$. The remaining parameter of the motion prediction module, the look-ahead time h, is chosen experimentally to minimize the error between the predicted and actual movement and was set here as $h = 126$ ms. The maximum displacement allowed for the gating of the transducer was determined experimentally as the value that would yield a lesion similar to the no-motion case and was set here as $\varepsilon = 1$ mm. The safety radius was set as $R_s = 20$ mm.

The execution time on an Intel i9-9900k processor was less than 1 ms for the motion tracking algorithm and around 12 ms for the motion prediction. All the scripts implemented here are available on request and are compatible with any URx e-series cobot model from Universal Robots.

E. Ex Vivo Experiments

The efficiency of the motion compensation approach presented here was tested in *ex vivo* BH treatments implemented in bovine heart tissue. Note that, although the BH system is intended for applications primarily in the liver and kidney, the heart tissue was chosen for testing to isolate only the influence of motion compensation on the BH lesion size and quality. This is due to its relative macroscopic homogeneity resulting in consistency of size and shape of BH lesions, as well as the ease of gross visual evaluation of the lesions [45]. The fresh bovine heart was obtained from a local abattoir on the day of the experiments and all testing occurred within 36 h from its receipt. The tissue was kept on ice during transportation and before the experiments. Prior to BH exposure, the heart was cut into cuboids of about 40 mm × 80 mm × 40 mm size, and pericardial fat, if any, was removed. The samples were then placed into cold degassed saline and degassed in a desiccant chamber for at least 1 h. Separately, an agarose gel was prepared by mixing agarose powder (UltraPure Agarose, Invitrogen) into deionized water (1.5% wt./vol. agarose/water). The resulting solution was then boiled for 10 min in a microwave oven to displace any dissolved gases present. The solution was then poured into a plastic mold of 80 mm × 50 mm × 50 mm size and cooled by placing the mold in a reservoir filled with cold water. Once the temperature of the gel reached 40 °C, the heart sample was placed into the mold, and the gel was left to polymerize for about 15 min. Once polymerized, the embedded sample was transferred into a custom-made sample holder with acoustic windows on its four rectangular sides.

The position of the sample holder was controlled by a 3-D positioning system (Velmex Inc, Bloomfield, NY, USA) within a tank filled with deionized water at room temperature and degassed to below 10% oxygen saturation. A polyurethane rubber acoustic absorber was placed about 6 cm behind the sample to avoid reverberation of HIFU and imaging waves. A photograph of the experimental setup is shown Fig. 5.

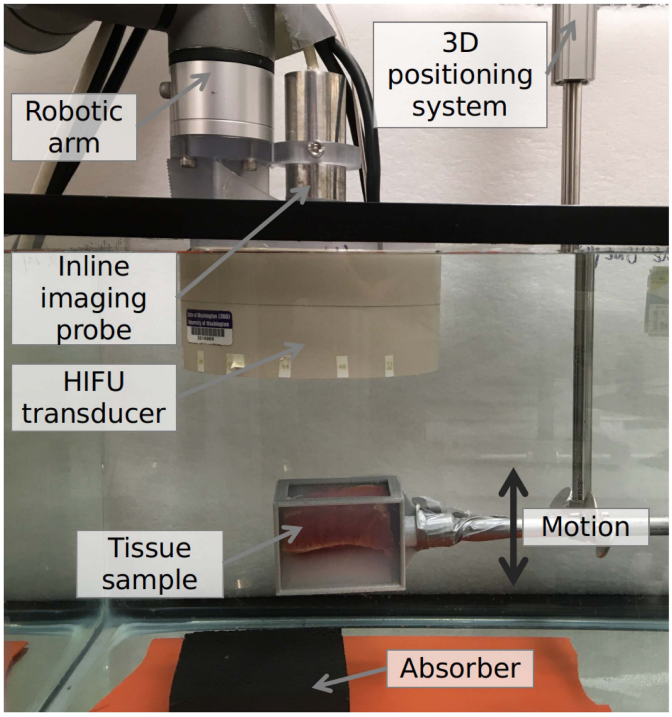

Fig. 5. Photograph of the experimental setup.

The experiments consisted of producing small volumetric BH lesions in the sample in three different scenarios: immobile sample, and moving sample with or without motion compensation activated. The volumetric BH treatment was performed by electronically steering the HIFU focus through a rectangular grid of 13 × 5 foci in a plane orthogonal to the axis of the HIFU array, centered around its geometric focus, with 1-mm spacing between the foci, which resulted in a total of 65 points treated. This specific pattern was selected following previous experiments with this transducer [38] and should result in a total ablated volume of approximately 15 mm × 7 mm × 6 mm. All the treatments were performed with the geometric focus of the HIFU transducer placed about 8 mm inside the tissue sample. The parameters of the BH treatments are given as follows: pulses of 10-ms duration, delivered at a PRF of 1 Hz, and each sonication point in the treatment plane received a single BH pulse before repeating the sonication, for a total of eight BH pulses per point. The voltage on the transducer elements was chosen before the treatment by delivering isolated BH pulses at escalating voltage to a different part of the tissue until a hyperechoic region was clearly visible on the B-mode imaging. The transducer voltage was then adjusted for every steered point according to previous methodology [38].

For the scenarios where the tissue sample was moving, the motion was introduced by controlling the 3-D positioning system along the same direction as the HIFU array axis. Three different motions, referenced as motions A, B, and C, were implemented, and their shape, period, and amplitude were based on previous observations during *in vivo* liver BH treatments in free-breathing porcine model from our group [18] and published data [35], [40], [41]. All the motion periods

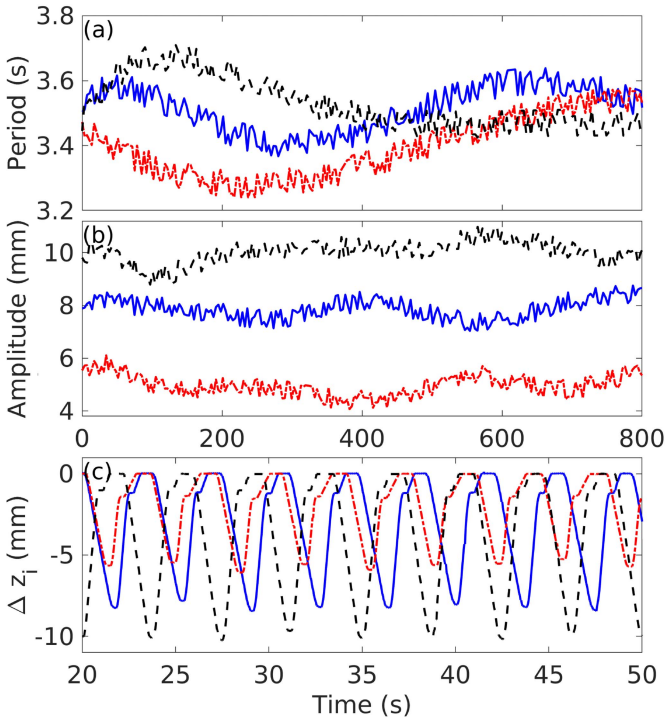

Fig. 6. Characteristics of the three modes of respiratory motions induced, with ▬ representing motion A, ▪▪▪ representing motion B, and ▪ ▪ ▪ representing motion C. (a) Period and (b) amplitude of the motion as a function of time. (c) 30-s-long excerpt of sample displacement as measured by the inline ultrasound imaging probe during treatments without motion compensation.

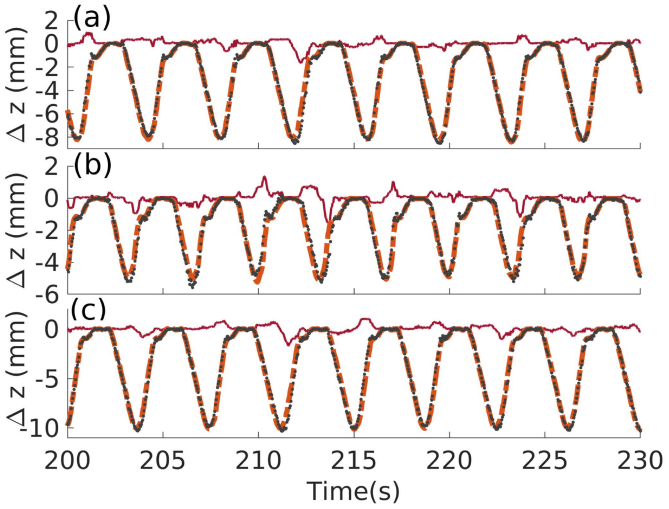

Fig. 7. 30-s-long excerpt of the sample surface displacement illustrating motion compensation for each mode of motion, where ▪▪▪▪▪ represents $\Delta\tilde{z}_i(t)$, ▬ represents $\Delta z_i(t)$, and ▪▪▪▪ represents $\Delta\hat{z}_i(t+h|t)$. (a) Motion A. (b) Motion B. (c) Motion C.

TABLE I
MOTION PARAMETERS

Motion	Period (s)	Amplitude (mm)	Peak inspiration speed (mm/s)	Peak expiration speed (mm/s)
A	3.48 ± 0.08	8 ± 0.43	5.74	11.7
B	3.41 ± 0.1	5.18 ± 0.48	5.59	9.9
C	3.51 ± 0.07	10 ± 0.38	7.82	14.2

TABLE II
MOTION COMPENSATION ERROR STATISTICS

Motion	RMS(Δz_i) (mm)	Maximum Δz_i (mm)
A (n=4)	0.39	4
B (n=2)	0.32	2.3
C (n=2)	0.42	3.1

and amplitudes had continuous and discontinuous variations over time, as shown in Fig. 6 and detailed in Table I.

III. RESULTS

In total, two BH treatments were performed without motion, four with and without motion compensation using motion A, and two with and without motion compensation using motions B and C each.

During the treatments with motion compensation, the values of the offset between the desired position of the water/sample interface and its actual position $\Delta z_i(t)$, the motion of the interface $\Delta\tilde{z}_i(t)$, and its predicted motion at instant $t+h$ $\Delta\hat{z}_i(t+h|t)$ were recorded, and a representative excerpt is presented in Fig. 7. The value of $\Delta z_i(t)$, while the motion compensation system was running, can be interpreted as the compensation error, and its statistics for the three types of motion are compiled in Table II.

The results of the motion compensation error statistics are presented in Table II and show that the root mean square (rms) values of the HIFU array focus position relative to the target was lower than half a millimeter for almost periodic movements with amplitudes within 5–10-mm range, indicating that the motion compensation was efficient. However, the variability, and thus unpredictability, of the amplitude and period of the movement resulted in short spikes of error, clearly visible in Fig. 7, which can reach values of up to 4 mm here. This demonstrates that gating of the BH pulses from the HIFU array, employed when the error was 1 mm or more, is complementary to the motion compensation to ensure the safety and accuracy of the treatment.

For every treatment, each time a BH pulse was emitted, the time and the offset of the interface Δz_i were recorded. The resulting treatment statistics are presented in Table III, with rms average and the maximum of Δz_i, the total treatment time, and the affected tissue length along the HIFU array axis z. The affected tissue length corresponding to the maximum length where gross tissue damages (whether mechanical or thermal) was visible and was measured on the gross histological cut using ImageJ [46]. The total treatment time increased for the cases with motion compensation as a result of gating the BH pulses. The benefit of the motion compensation and gating system on the *ex vivo* treatment efficiency was a reduction of the targeting error (rms average of Δz_i) by 92%, 89%, and 93% for motions A, B, and C, respectively, while only making the treatment no more than 1% longer in all cases.

Photographs of the bisected BH lesions produced during treatments without any motion, treatments with motion and treatments with motion, and the motion compensation system activated are presented in Fig. 8. In all cases, the liquefied

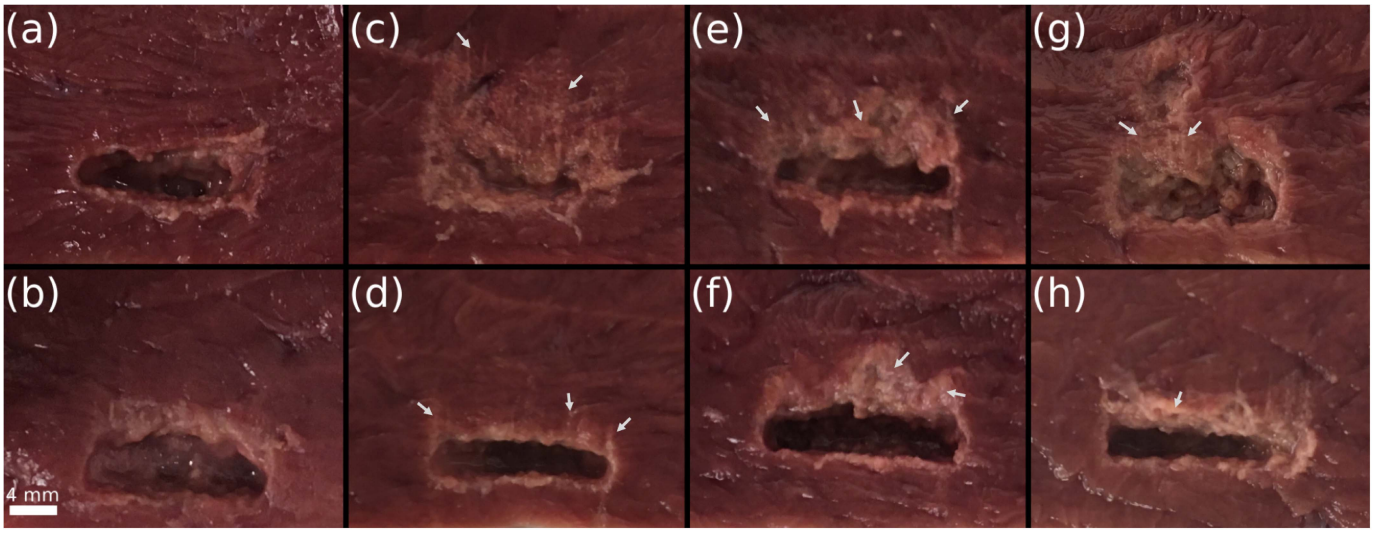

Fig. 8. Gross evaluation of the volumetric BH lesions under different motion conditions. The cut was made perpendicular to the imaging/treatment plane and along the largest width of the treatment plane. The liquefied tissues present were delicately washed out prior to the photographs were taken. The BH treatment was from the bottom of the frames. (a) and (b) No motion during the treatment. (c) and (d) Treatments under motion A (c) without motion compensation and (d) with motion compensation. (e) and (f) Treatments under motion B (e) without motion compensation and (f) with motion compensation. (g) and (h) Treatments under motion C (g) without motion compensation and (h) with motion compensation. The white arrows designate examples of thermal damage.

TABLE III
TREATMENTS STATISTICS

Treatment	RMS Δz_i (mm)	max Δz_i (mm)	Total time (s)	Affected tissue length along z (mm)
Without motion (n=2)	0	0	520	6.5±0.5
A without compensation (n=4)	4.1	9.2	520	12.6±0.9
B without compensation (n=2)	2.5	5.8	520	9.9±0.5
C without compensation (n=2)	5.2	11	520	13.8±2.3
A with compensation (n=4)	0.33	1	525.7±1	7.1±0.7
B with compensation (n=2)	0.27	0.97	524±0.1	7.5±1.3
C with compensation (n=2)	0.35	0.98	525.2±1	8.1±0.2

tissue content inside the lesions could be easily washed out using saline.

The lesions produced in the immobile samples had sharp and smooth boundaries, with a blanched rim of width ranging within 1–2 mm around the edges, which was observed previously in BH treatments of the bovine heart. The rim most probably represented partially fractionated tissue resulting from the incomplete merging of the distal "tails" of the BH lesions. The lesions produced in moving samples without motion compensation had lumps of untreated tissues mixed in with the liquefied debris and an overall larger affected region compared to the immobile case—94%, 52%, and 112% larger for motions A, B, and C, respectively. With motion compensation and compared to the no motion case, the affected tissue lengths were only 9%, 15%, and 25% larger for motions A, B, and C, respectively. The treatments with motion compensation yielded lesions of similar size and quality as those produced in immobile samples albeit with a wider (by 1–3 mm) blanched rim along the distal side of the lesion, with occasional narrow areas characteristic of either thermal damage or changes in heme iron associated with lower temperature increases, as observed in BH lesions previously [45]. This thermal effect on the distal side could be the result of occasional positioning of the focus behind the lesion within the margin allowed by the motion compensation and gating algorithm (1-mm maximum for the motion compensation case here with the gating setting) and accentuated attenuation caused by prefocal cavitation inside the liquefied tissue—caused by bubble nuclei from previous treatment point—preventing the formation of a boiling bubble at that point [18], [47].

Videos documenting treatments under motion C are available in the Multimedia File in the Supplementary Material. One video shows the treatment without motion compensation (no_compensation.mp4), and another one shows the treatment with motion compensation (motion_compensation.mp4). The boiling bubbles resulting from the BH treatment are visible on the B-mode images as 1-mm-diameter hyperechoic regions [15].

IV. CONCLUSION AND DISCUSSION

In this article, a practical way of active compensation for the respiratory motion during BH treatment was described and implemented. While it only offers a partial compensation of the respiratory motion during treatment due to the fact that the skin is used as a reference for tracking, its implementation does not require any changes to the HIFU system and is fast and simple to implement. The robotic arm used in this work is relatively affordable and performs well in matching the speed of respiratory motion and in terms of precision and accuracy of the movement. Being a cobot, it also offers hardware safety settings that allow it to maneuver safely around the staff and animal/patient treated.

As the B-mode imaging frame rate was 27.5 Hz here, similar results could be obtained by using a commercial ultrasound

imaging system with a similar frame rate and a frame grabber instead of the Verasonics setup used here. As the tracking is interpolated in time in the motion prediction module, even lower values of a B-mode frame rate would suffice, as long as the motion of the skin is spatially resolved decently; the simplicity of the tracking algorithm allows for tracking the water/tissue interface even with suboptimal imaging quality at the focal area of the transducer.

An SAR motion prediction algorithm was used here in order to compensate for any response time between the ultrasound imaging acquisition and the robot. This also allows for flexibility in the implementation as even longer response time than presented here, for example, resulting from a lower B-mode frame rate in the case of using an image grabber with a clinical ultrasound imaging system, should be efficiently compensated as well. Unfortunately, being an autoregressive algorithm, it does not deal well with sudden pattern changes, as it could happen for *in vivo* cases with an unexpected movement from the patient. However, the transducer gating implemented here would make sure that the treatment is paused in that case, both ensuring the safety of the patient and the transducer. The sudden error increase from this event could also be easily detected and dealt with by resetting the motion prediction algorithm.

The HIFU transducer could also be of any type, e.g., single-element transducer or a phased array as used here, as long as the transducer allows for inline ultrasound imaging. While not implemented here, changing the position of the transducer to mechanically ablate a volume—instead of electronically steering as in this work—while keeping the motion compensation and gating operational, is a possibility.

The implemented motion tracking uses the skin/water rather than the targeted area at the focus of the HIFU transducer. This was done to avoid tracking issues at the ROI as a consequence of the low SNR of B-mode imaging, out-of-plane motion, and transient and chaotic echogenicity changes due to bubble motion within the liquefied area following each BH pulse. As such, a comparison of the algorithm's performance characteristics with other methods designed for thermal HIFU present in the literature would be difficult. *Ex vivo* experiments showed a net improvement of the treatment precision and completeness under simulated, unidirectional respiratory motion when the developed motion compensation system was used by creating lesions similar in dimensions and quality to a no-motion case. In the present case, the gating ensured that the compensation error was always less than a millimeter when emitting a BH pulse. Another important point here is that the actual precision of the motion compensation system can be easily customized to the need of the user by changing the gating value. However, using a gating limit close or even inferior to the rms of the compensation error would result in a more significant increase in the treatment time than observed in this work.

The movement compensation presented here was implemented only in one direction—along the HIFU transducer axis—which means that the respiratory motion would only be compensated partially. Depending on the organ targeted, the subject positioning, the position of the transducer, and even the region in the organ targeted, the efficiency of this approach may vary. As such, *in vivo* testing of this system on free-breathing anesthetized pigs will follow in order to obtain realistic values of the total respiratory compensation resulting from this approach and its benefit on BH ablation precision.

Finally, while the system was conceived with BH treatments in mind, it could be easily adapted to shock scattering histotripsy as it also consists of short pulses emitted at a low duty cycle, allowing for ultrasonic imaging. Application to thermal HIFU is also a possibility but will require the use of an interleaved HIFU/imaging scheme, similar to the ones proposed in [28] and [29].

REFERENCES

[1] F. Wu *et al.*, "Extracorporeal high intensity focused ultrasound ablation in the treatment of patients with large hepatocellular carcinoma," *Ann. Surg. Oncol.*, vol. 11, no. 12, p. 1061, 2004.

[2] R. O. Illing *et al.*, "The safety and feasibility of extracorporeal high-intensity focused ultrasound (HIFU) for the treatment of liver and kidney tumours in a western population," *Brit. J. Cancer*, vol. 93, no. 8, pp. 890–895, Oct. 2005.

[3] F. Wu, G. ter Haar, and W. R. Chen, "High-intensity focused ultrasound ablation of breast cancer," *Expert Rev. Anticancer Therapy*, vol. 7, no. 6, pp. 823–831, Jun. 2007.

[4] L. G. Merckel *et al.*, "First clinical experience with a dedicated MRI-guided high-intensity focused ultrasound system for breast cancer ablation," *Eur. Radiol.*, vol. 26, no. 11, pp. 4037–4046, Nov. 2016.

[5] J. H. Hwang *et al.*, "Preclinical *in vivo* evaluation of an extracorporeal HIFU device for ablation of pancreatic tumors," *Ultrasound Med. Biol.*, vol. 35, no. 6, pp. 967–975, Jun. 2009.

[6] W. Chang *et al.*, "A portable high-intensity focused ultrasound system for the pancreas with 3D electronic steering: A preclinical study in a swine model," *Ultrasonography*, vol. 37, no. 4, p. 298, 2018.

[7] R. W. Ritchie *et al.*, "Extracorporeal high intensity focused ultrasound for renal tumours: A 3-year follow-up: Extracorporeal HIFU For renal tumours," *BJU Int.*, vol. 106, no. 7, pp. 1004–1009, Oct. 2010.

[8] C. Yiallouras and C. Damianou, "Review of MRI positioning devices for guiding focused ultrasound systems," *Int. J. Med. Robot. Comput. Assist. Surg.*, vol. 11, no. 2, pp. 247–255, Jun. 2015.

[9] G. ter Haar and C. Coussios, "High intensity focused ultrasound: Physical principles and devices," *Int. J. Hyperthermia*, vol. 23, no. 2, pp. 89–104, Jan. 2007.

[10] Z. Xu *et al.*, "Controlled ultrasound tissue erosion," *IEEE Trans. Ultrason., Ferroelectr., Freq. Control*, vol. 51, no. 6, pp. 726–736, Jun. 2004.

[11] T. D. Khokhlova, M. S. Canney, V. A. Khokhlova, O. A. Sapozhnikov, L. A. Crum, and M. R. Bailey, "Controlled tissue emulsification produced by high intensity focused ultrasound shock waves and millisecond boiling," *J. Acoust. Soc. Amer.*, vol. 130, no. 5, pp. 3498–3510, Nov. 2011.

[12] J. C. Simon, O. A. Sapozhnikov, V. A. Khokhlova, Y.-N. Wang, L. A. Crum, and M. R. Bailey, "Ultrasonic atomization of tissue and its role in tissue fractionation by high intensity focused ultrasound," *Phys. Med. Biol.*, vol. 57, no. 23, p. 8061, 2012.

[13] K. J. Pahk, P. Gélat, D. Sinden, D. K. Dhar, and N. Saffari, "Numerical and experimental study of mechanisms involved in boiling histotripsy," *Ultrasound Med. Biol.*, vol. 43, no. 12, pp. 2848–2861, Dec. 2017.

[14] D. Melodelima, W. A. N'Djin, N. R. Miller, J. C. Bamber, and J.-Y. Chapelon, "Comparative study of the effects of respiratory motion on *in-vivo* HIFU treatments in the liver," in *Proc. IEEE Int. Ultrason. Symp.*, Sep. 2009, pp. 1314–1317.

[15] T. D. Khokhlova *et al.*, "Ultrasound-guided tissue fractionation by high intensity focused ultrasound in an *in vivo* porcine liver model," *Proc. Nat. Acad. Sci. USA*, vol. 111, no. 22, pp. 8161–8166, Jun. 2014.

[16] Y. Kim, E. Vlaisavljevich, G. Owens, S. Allen, C. Cain, and Z. Xu, "In vivo transcostal histotripsy therapy without aberration correction," *Phys. Med. Biol.*, vol. 59, no. 11, p. 2553, 2014.

[17] E. Vlaisavljevich *et al.*, "Non-invasive liver ablation using histotripsy: Preclinical safety study in an *in vivo* porcine model," *Ultrasound Med. Biol.*, vol. 43, no. 6, pp. 1237–1251, Jun. 2017.

[18] T. D. Khokhlova *et al.*, "Pilot *in vivo* studies on transcutaneous boiling histotripsy in porcine liver and kidney," *Sci. Rep.*, vol. 9, no. 1, Dec. 2019, Art. no. 20176.

[19] A. Okada *et al.*, "A case of hepatocellular carcinoma treated by MR-guided focused ultrasound ablation with respiratory gating," *Magn. Reson. Med. Sci.*, vol. 5, no. 3, pp. 167–171, 2006.

[20] F. Wu *et al.*, "Advanced hepatocellular carcinoma: Treatment with high-intensity focused ultrasound ablation combined with transcatheter arterial embolization," *Radiology*, vol. 235, no. 2, pp. 659–667, May 2005.

[21] A. Muller, L. Petrusca, V. Auboiroux, P. J. Valette, R. Salomir, and F. Cotton, "Management of respiratory motion in extracorporeal high-intensity focused ultrasound treatment in upper abdominal organs: Current status and perspectives," *CardioVascular Interventional Radiol.*, vol. 36, no. 6, pp. 1464–1476, Dec. 2013.

[22] R. Ginhoux, J. Gangloff, M. de Mathelin, L. Soler, M. M. A. Sanchez, and J. Marescaux, "Active filtering of physiological motion in robotized surgery using predictive control," *IEEE Trans. Robot.*, vol. 21, no. 1, pp. 67–79, Feb. 2005.

[23] V. Auboiroux *et al.*, "Respiratory-gated MRgHIFU in upper abdomen using an MR-compatible in-bore digital camera," *BioMed Res. Int.*, vol. 2014, pp. 1–9, Jan. 2014.

[24] B. D. de Senneville, C. Mougenot, and C. T. W. Moonen, "Real-time adaptive methods for treatment of mobile organs by MRI-controlled high-intensity focused ultrasound," *Magn. Reson. Med.*, vol. 57, no. 2, pp. 319–330, 2007.

[25] B. Stemkens, R. H. Tijssen, B. D. De Senneville, J. J. Lagendijk, and C. A. VanDen Berg, "Image-driven, model-based 3D abdominal motion estimation for MR-guided radiotherapy," *Phys. Med. Biol.*, vol. 61, no. 14, p. 5335, 2016.

[26] A. Diodato, A. Cafarelli, A. Schiappacasse, S. Tognarelli, G. Ciuti, and A. Menciassi, "Motion compensation with skin contact control for high intensity focused ultrasound surgery in moving organs," *Phys. Med. Biol.*, vol. 63, no. 3, Jan. 2018, Art. no. 035017.

[27] A. Krupa, G. Fichtinger, and G. D. Hager, "Real-time motion stabilization with B-mode ultrasound using image speckle information and visual servoing," *Int. J. Robot. Res.*, vol. 28, no. 10, pp. 1334–1354, 2009.

[28] L.-A. Chanel, F. Nageotte, J. Vappou, J. Luo, L. Cuvillon, and M. de Mathelin, "Robotized high intensity focused ultrasound (HIFU) system for treatment of mobile organs using motion tracking by ultrasound imaging: An *in vitro* study," in *Proc. 37th Annu. Int. Conf. IEEE Eng. Med. Biol. Soc. (EMBC)*, Aug. 2015, pp. 2571–2575.

[29] J. Seo, N. Koizumi, M. Mitsuishi, and N. Sugita, "Ultrasound image based visual servoing for moving target ablation by high intensity focused ultrasound," *Int. J. Med. Robot. Comput. Assist. Surg.*, vol. 13, no. 4, p. e1793, Dec. 2017.

[30] M. Pernot, M. Tanter, and M. Fink, "3-D real-time motion correction in high-intensity focused ultrasound therapy," *Ultrasound Med. Biol.*, vol. 30, no. 9, pp. 1239–1249, Sep. 2004.

[31] A. H. Gee, R. James Housden, P. Hassenpflug, G. M. Treece, and R. W. Prager, "Sensorless freehand 3D ultrasound in real tissue: Speckle decorrelation without fully developed speckle," *Med. Image Anal.*, vol. 10, no. 2, pp. 137–149, Apr. 2006.

[32] J. Seo *et al.*, "Biplane US-guided real-time volumetric target pose estimation method for theragnostic HIFU system," *J. Robot. Mechatronics*, vol. 23, no. 3, pp. 400–407, Jun. 2011.

[33] J. Seo *et al.*, "Visual servoing for a US-guided therapeutic HIFU system by coagulated lesion tracking: A phantom study," *Int. J. Med. Robot. Comput. Assist. Surg.*, vol. 7, no. 2, pp. 237–247, Jun. 2011.

[34] M. A. Clifford, F. Banovac, E. Levy, and K. Cleary, "Assessment of hepatic motion secondary to respiration for computer assisted interventions," *Comput. Aided Surg.*, vol. 7, no. 5, pp. 291–299, Jan. 2002.

[35] G. Srimathveeravalli, J. Leger, P. Ezell, M. Maybody, N. Gutta, and S. B. Solomon, "A study of porcine liver motion during respiration for improving targeting in image-guided needle placements," *Int. J. Comput. Assist. Radiol. Surg.*, vol. 8, no. 1, pp. 15–27, Jan. 2013.

[36] V. A. Khokhlova *et al.*, "Design of HIFU transducers to generate specific nonlinear ultrasound fields," *Phys. Procedia*, vol. 87, pp. 132–138, Apr. 2016.

[37] M. A. Ghanem *et al.*, "Field characterization and compensation of vibrational nonuniformity for a 256-element focused ultrasound phased array," *IEEE Trans. Ultrason., Ferroelectr., Freq. Control*, vol. 65, no. 9, pp. 1618–1630, Sep. 2018.

[38] C. R. Bawiec *et al.*, "A prototype therapy system for boiling histotripsy in abdominal targets based on a 256-element spiral array," *IEEE Trans. Ultrason., Ferroelectr., Freq. Control*, early access, Nov. 6, 2020, doi: 10.1109/TUFFC.2020.3036580.

[39] T. Fujii *et al.*, "Servoing performance enhancement via a respiratory organ motion prediction model for a non-invasive ultrasound theragnostic system," *J. Robot. Mechtron.*, vol. 29, no. 2, pp. 434–446, Apr. 2017.

[40] L. Maier-Hein *et al.*, "On combining internal and external fiducials for liver motion compensation," *Comput. Aided Surg.*, vol. 13, no. 6, pp. 369–376, Jan. 2008.

[41] J. Fehrenbach, M. Masmoudi, and D. Melodelima, "Low dimensional optimization for *in vivo* real-time porcine liver motion estimation using ultrasound imaging," *Ultrasonics*, vol. 50, no. 1, pp. 44–51, Jan. 2010.

[42] K. Ichiji *et al.*, "A time-varying seasonal autoregressive model-based prediction of respiratory motion for tumor following radiotherapy," *Comput. Math. Methods Med.*, vol. 2013, pp. 1–9, Jun. 2013.

[43] K. Hatada, K. Hirata, and T. Sato, "Power assisting method for almost-periodic motions based on motion prediction," in *Proc. IEEE Int. Conf. Ind. Technol.*, Dec. 2015, pp. 417–422.

[44] M. Cejnek. *Python Adaptive Signal Processing*. Accessed: Aug. 21, 2021. [Online]. Available: http://matousc89.github.io/padasip/

[45] Y.-N. Wang, T. Khokhlova, M. Bailey, J. H. Hwang, and V. Khokhlova, "Histological and biochemical analysis of mechanical and thermal bioeffects in boiling histotripsy lesions induced by high intensity focused ultrasound," *Ultrasound Med. Biol.*, vol. 39, no. 3, pp. 424–438, Mar. 2013.

[46] C. A. Schneider, W. S. Rasband, and K. W. Eliceiri, "NIH image to ImageJ: 25 years of image analysis," *Nature Methods*, vol. 9, no. 7, pp. 671–675, Jul. 2012.

[47] T. D. Khokhlova, Y. A. Haider, A. D. Maxwell, W. Kreider, M. R. Bailey, and V. A. Khokhlova, "Dependence of boiling histotripsy treatment efficiency on HIFU frequency and focal pressure levels," *Ultrasound Med. Biol.*, vol. 43, no. 9, pp. 1975–1985, Sep. 2017.

Gilles P. L. Thomas received the Engineering degree in general engineering from the École Centrale de Nantes, Nantes, France, in 2014, the Engineering degree in mechatronics engineering and the M.S. degree in control and automation engineering from the Polytechnic School, University of São Paulo, São Paulo, Brazil, in 2014 and 2015, respectively, and the Ph.D. degree in biomedical engineering from Université Lyon 1, Lyon, France, in 2019.

He is currently pursuing a post-doctoral training at the Applied Physics Laboratory, University of Washington, Seattle, WA, USA.

Tatiana D. Khokhlova received the Ph.D. degree in physics from Moscow State University (MSU), Moscow, Russia, in 2008.

After graduation from the Ph.D. program, she moved to the University of Washington (UW), Seattle, WA, USA, for post-doctoral training at the Applied Physics Laboratory, and then completed a research fellowship at the Department of Medicine. She is currently an Associate Professor with the Department of Medicine, UW. Her research interests are in physical acoustics, therapeutic ultrasound, and photoacoustic imaging.

Vera A. Khokhlova received the M.S. degree in physics and the Ph.D. and D.Sc. degrees in acoustics from Moscow State University (MSU), Moscow, Russia, in 1986, 1991, and 2012, respectively.

After graduation from the Ph.D. program, she was appointed by the MSU, where she is currently an Associate Professor with the Department of Acoustics, Physics Faculty. Since 1995, she has been with the Applied Physics Laboratory (APL), Center for Industrial and Medical Ultrasound, University of Washington, Seattle, WA, USA. Her research interests are in the fields of nonlinear acoustics, therapeutic ultrasound, including metrology and bioeffects of high-intensity focused ultrasound fields, shock wave focusing, nonlinear wave propagation in inhomogeneous media, and nonlinear modeling.